NANO LETTERS

pubs.acs.org/NanoLett

Letter

Hybrid Metal-Dielectric Metasurfaces for Refractive Index Sensing

Debdatta Ray, T. V. Raziman, Christian Santschi, Dordaneh Etezadi, Hatice Altug, and Olivier J. F. Martin*

Cite This: *Nano Lett.* 2020, 20, 8752−8759

Read Online

ACCESS | Metrics & More | Article Recommendations | Supporting Information

ABSTRACT: Hybrid metal-dielectric nanostructures have recently gained prominence because they combine strong field enhancement of plasmonic metals and the several low-loss radiation channels of dielectric resonators, which are qualities pertaining to the best of both worlds. In this work, an array of such hybrid nanoantennas is successfully fabricated over a large area and utilized for bulk refractive index sensing with a sensitivity of 208 nm/RIU. Each nanoantenna combines a Si cylinder with an Al disk, separated by a SiO_2 spacer. Its optical response is analyzed in detail using the multipoles supported by its subparts and their mutual coupling. The nanoantenna is further modified experimentally with an undercut in the SiO_2 region to increase the interaction of the electric field with the background medium, which augments the sensitivity to 245 nm/RIU. A detailed multipole analysis of the hybrid nanoantenna supports our experimental findings.

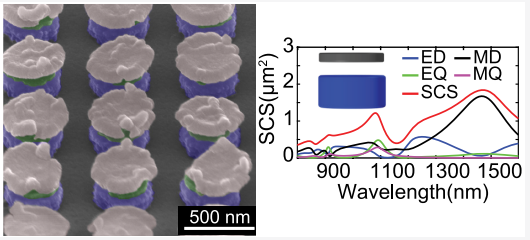

KEYWORDS: *Hybrid nanoantenna, hybridization, LSPR, bulk refractive index sensing, undercut*

INTRODUCTION

Plasmonic nanostructures exhibit strong electric field enhancement caused by the resonant oscillation of free electrons.[1,2] Unfortunately, the intrinsic absorption associated with plasmonic metals results in high losses, which represent a serious drawback for practical applications.[3] To overcome this problem, dielectric nanostructures, which exhibit modest losses but also lower field enhancement, have been recently proposed.[1,4−8] Furthermore, to take advantage of both low losses and high field enhancement, hybrid metal-dielectric nanostructures, which combine the advantages of both the plasmonic and dielectric properties, are emerging as a promising approach. It has been theoretically predicted that hybrid nanostructures acting as nanoantennas provide high directivity and radiation enhancement[9−11] and are potential candidates for fluorescence enhancement.[9,11−13]

However, there is a dearth of experimental demonstrations with these hybrid nanoantennas, probably because their fabrication is extremely difficult. The unidirectional radiation of light from hybrid metasurfaces[14,15] and hybrid Yagi-Uda nanoantennas[16] has been experimentally demonstrated. Experiments have been conducted with quantum dots (QDs) to show the directionality of the hybrid nanoantennas[17] and the increment of the decay rate of the QDs.[18] Hybrid metal-dielectric nanoantennas have also been used for subtractive color filtering[19] and efficient generation of second[20] and third harmonics.[21] Hentschel et al. have studied the linear and nonlinear optical properties of a hybrid metal dielectric nanoantenna made of Au bow tie nanoantenna with $LiNbO_3$ nanoparticles in the gap.[22] Additional nanostructures that combine more than one material include heterodimers[23−25] and core−shell particles.[26,27]

In this Letter, we are concerned with hybrid nanostructures that combine in themselves a dielectric and a metallic part with a fabrication friendly sandwich design and demonstrate experimentally these nanoantennas as candidates for biosensing. The world of biosensing is mainly dominated by plasmonic biosensors, especially surface plasmon-polaritons (SPPs) or propagating plasmon resonances, yielding an experimental bulk sensitivity of 5.9×10^4 nm/RIU[28,29] and around 2×10^5 nm/RIU predicted theoretically.[29−31] Localized surface plasmon resonance (LSPR) sensors, based on plasmonic nanoantennas, can potentially be used for point of care testing thanks to their miniature size.[29,32,33] Although their sensitivity is lower than SPP sensors, values taken from ref 29 for bulk refractive index sensing are in the order of 400−600 nm/RIU for LSPR sensors. On the other hand, dielectric sensors reach a typical bulk sensitivity up to 300 nm/RIU.[34−36]

We investigate the sensing performances of metasurfaces consisting of hybrid nanoantennas built by a sandwich structure of an Al disk and a Si cylinder separated by a SiO_2 spacer. This hybrid nanoantenna is fabricated by e-beam lithography and dry etching of the SiO_2 and Si. We compute

Received: September 7, 2020
Revised: November 6, 2020
Published: November 18, 2020

https://dx.doi.org/10.1021/acs.nanolett.0c03613
Nano Lett. 2020, 20, 8752−8759

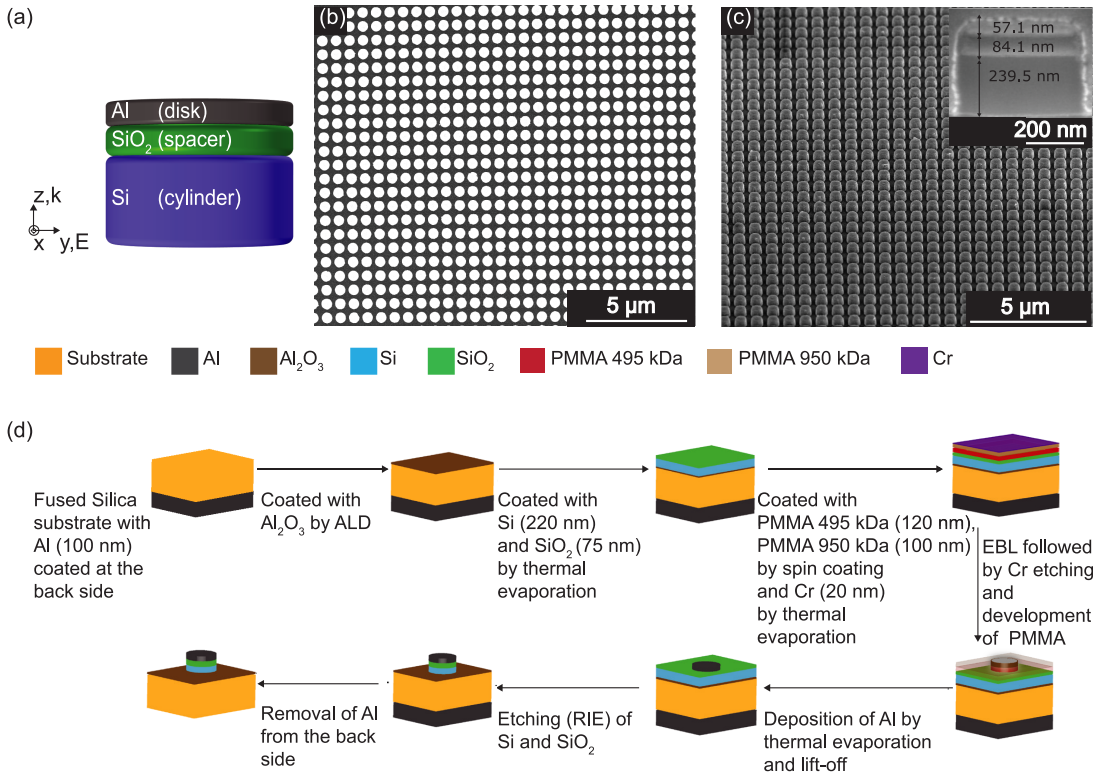

Figure 1. (a) Geometry of the hybrid metal-dielectric nanoantenna. k denotes the propagation direction of the incident wave, whereas E denotes the direction of the electric field. SEM images of the nanoantenna array with a period of 670 nm: (b) top view and (c) 52° tilt; the inset shows the cross-section, made by FIB etching, of a single nanoantenna. (d) Process flow for the fabrication of the hybrid nanoantenna.

the scattering properties of the nanostructure, conduct a multipolar analysis by decomposing the optical field into vector spherical harmonics, and interpret the response of the hybrid system in terms of the scattering of its separate components, thus providing an understanding of the working principles of the hybrid nanoantenna. A refined nanofabrication technology is developed to produce hybrid structures on a large area and experimental results demonstrate the applications of this hybrid nanoantenna for bulk refractive index sensing. Combining different etching approaches, we further extend the nanofabrication to nanoantennas with an undercut to favor near-field interactions between the structure and the analyte. This work paves the path for hybrid geometries being incorporated as refractive index sensors.

NANOFABRICATION

Figure 1a shows the geometry of the hybrid metal-dielectric nanoantenna, which represents the building block or meta-atom for the hybrid metasurface. The nanoantenna with a diameter of 470 nm, consists of a 220 nm thick Si cylindrical base covered with a 60 nm thick Al cylindrical cap; a 75 nm thick SiO_2 spacer is introduced between the Si and the Al to control their near-field interaction. There is a recent effort to use Al in plasmonics because of its low cost, high abundance in nature, compatibility with CMOS processes,[35,37−39] and chemical stability due to self-limiting oxide layer. Since Al and Si are CMOS compatible materials, such hybrid nanoantennas can potentially be integrated into optoelectronic CMOS chips.[40] Note that Al is the key for the fabrication process used in this study, because it serves as a hard mask for the dry etching of pure Si and SiO_2 and as a plasmonic component.

The process developed in this study is intended for the fabrication of large area samples, typically 200 × 200 μm^2, that are suitable for realistic sensing applications.[8,41,42] Figure 1 shows a sample under normal view (panel b) and 52° tilt (panel c). The SEM image of an area containing over 700 nanoantennas shows a very high level of fabrication uniformity. The different process steps are detailed in Figure 1d. The hybrid nanoantennas are fabricated on a fused silica substrate which is coated with 100 nm Al at the back to ensure electrostatic clamping of the wafer for etching of the Si and SiO_2 at later stages. Ten nanometers thick Al_2O_3 is deposited by atomic layer deposition (ALD BENEQ TFS200) on the substrate to serve as a stopping layer for the HF vapor dry etch, which is used later to modify the antennas by undercutting the SiO_2 spacer layer. This is followed by the evaporation (Leybold Optics LAB 600H) of pure Si and SiO_2 with 220 and 75 nm thicknesses, respectively. Two layers of electron beam resist PMMA (Microresist Technology GmbH) with different molecular weights: first 120 nm with 495 kDa and second 100 nm with 950 kDa are subsequently spin-coated on the SiO_2. Because the substrate is fused silica, 20 nm of Cr is deposited on top of the PMMA to dissipate the charges during electron beam lithography. After electron beam lithography (EBL), Cr is removed using wet-etching (18 s in TechniEtch Cr01 at room temperature) prior to the development of the PMMA. The Al nanodisks are realized by lift-off technique consisting of Al deposition using an AgO_x seed layer to improve the quality of the Al structures, as described in ref 32. Because the Al disks are used as a hard mask for deep reactive ion etching (RIE) to define the underlying SiO_2 and Si structures but also as a plasmonic component, a relatively thick Al layer of 60 nm is deposited. The reactive ion etching is

https://dx.doi.org/10.1021/acs.nanolett.0c03613
Nano Lett. 2020, 20, 8752−8759

performed using Alcatel AMS 200 SE dry etcher with fluorine chemistry. To remove Al from the backside using wet-etching (ANP VLSI at 35 °C), the entire wafer top surface is protected by coating with 1 μm thick photoresist AZ 1512 (Micro-Chemicals at 6000 rpm, postbake at 100 °C for 1 min). Finally, the protective photoresist is removed (two runs in Remover 1165 for 5 min each at 70 °C) giving rise to the final hybrid metal-dielectric nanoantennas shown in Figure 1b,c.

MULTIPOLE ANALYSIS

In order to study the working principle of the proposed design, we first simulated the nanostructures by multipole analysis. In particular, the interplay of the different modes supported by the structure is investigated by considering a single hybrid nanoantenna under normal incidence since multipole analysis cannot be performed on a periodic system. The illumination condition is shown in Figure 1a. The refractive index of Al has been taken from ref 32 and that of Si from ref 43. First, the scattering cross-section for the different structures is computed using the full wave surface integral equation method and shown as red curves in Figure 2.[44,45] The radiated electromagnetic field computed for the different structures is then used to perform a multipole decomposition into vector spherical harmonics.[46−48] The electric dipole (ED), electric quadrupole (EQ), magnetic dipole (MD), and magnetic quadrupole (MQ) are sufficient to build the entire response of the system (i.e., the scattering cross-section can be decomposed into those four modes as shown in Figure 2). The scattering cross section of the nanoantenna along with the contribution from the individual multipoles are indicated by the y-axis. The calculation reveals that the Al disk has a broad electric dipole, whereas the Si cylinder has additional higher order multipoles such as a magnetic dipole and electric quadrupole, which agrees with previous studies on Si cylinders.[49] Upon combining them, the interaction of the Al disk with the Si cylinder gives rise to a large number of higher order multipoles like electric and magnetic quadrupoles and magnetic dipole in addition to the lower order electric dipole. This results in a spectrum with multiple features as seen in Figure 2c.

In order to understand how the Al disk and Si cylinder contribute to the total response in greater detail, we have computed in Figure 2d the multipole decomposition by considering separately the Al disk and the Si cylinder. This is done by taking the surface currents obtained when the entire hybrid structure is illuminated but computing the scattered fields from each separate subpart, ignoring the other one, and performing a multipole decomposition of that scattered field. Let us consider three scattering peak wavelengths of the hybrid structure λ = 916 nm, λ = 1080 nm, and λ = 1472 nm (Figure 2c) to illustrate the interplay of the different modes. At λ = 916 nm, we observe in Figure 2d strong EQ and MD coming from the Si cylinder; however, these two modes are weaker for the hybrid structure (Figure 2c). This is because the EDs from the Al disk and the Si cylinder are out of phase and thus give rise to an EQ and a MD that interfere with those contributed by the Si cylinder,[50] leading to reduced moments for the hybrid system. At λ = 1080 nm, we observe in Figure 2d that both the Si cylinder and the Al disk produce very strong ED, whereas ED is reduced in the hybrid system in Figure 2c, where a sizable MQ is also visible. This can be explained by partial cancellation of the EDs from the Al disk and the Si cylinder because they are out of phase, leading to enhanced EQ and

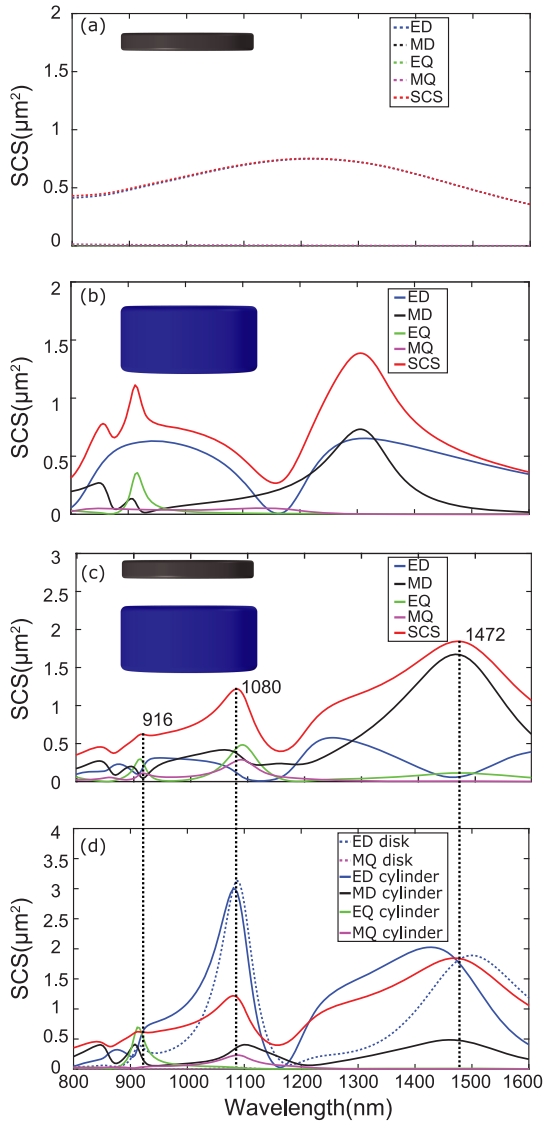

Figure 2. Multipole decomposition using vector spherical harmonics for a single (a) 60 nm thick Al disk, (b) 220 nm thick Si cylinder, and (c) hybrid nanoantenna comprising these two elements with a 75 nm thick air spacer. ED, MD, EQ and MQ denote the electric dipole, the magnetic dipole, the electric quadrupole and the magnetic quadrupole, respectively. (d) Contribution of the different multipoles from the Al disk and the Si cylinder to that of the hybrid nanostructure. The red curves in (a−d) represent the scattering cross-section of the nanostructure, which is equal to the sum of all the multipoles considered. The individual multipoles in (c) are decomposed in (d) where the contributions from the Al disk and the Si cylinder are plotted separately.

MD in the hybrid system. This resulting MD interacts with the MD of the Si disk, increasing the net MD as well as the MQ in the hybrid structure, whereas the enhanced EQ increases the resulting EQ. At λ = 1472 nm, we see from Figure 2d that the EDs from both the Si cylinder and the Al disk are the respective dominant multipoles, whereas in the case of the hybrid structure in Figure 2c the MD is dominant. This dominant MD along with the weaker EQ results from the interaction between the individual ED moments from the Al and Si subparts, leaving the resulting ED in the coupled system to be small. This illustrates how the interaction of a dielectric

https://dx.doi.org/10.1021/acs.nanolett.0c03613
Nano Lett. 2020, 20, 8752−8759

with a metal results in an abundance of spectral features, is a quality unseen in metal alone.

To assess the suitability of this hybrid nanoantenna as a localized refractive index sensor, we first compute in Figure 3

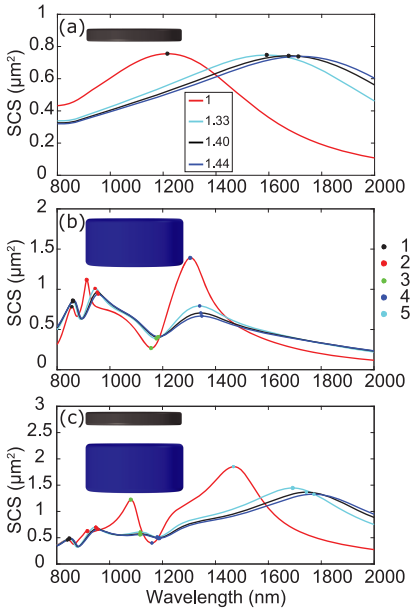

Figure 3. Simulations for (a) a 60 nm thick Al disk, (b) a 220 nm thick Si cylinder, and (c) the hybrid nanoantenna comprising these two elements with a 75 nm thick air spacer for four different background refractive indices corresponding to different mass percentages of glucose in the solution. The evolution of 1 (panel a), 4 (panel b), or 5 (panel c) spectral features as a function of the background is indicated with colored dots and corresponds to the values reported in Table SI 1.

the spectra of a single nanoantenna and its two supbarts for four different surrounding media: air (n = 1), water (n = 1.33), water with 42% mass glucose (n = 1.40), and water with 60% mass glucose (n = 1.44). The sensitivity (S) = $\Delta\lambda/\Delta n$ calculated from these plots for the different spectral features are shown in Table SI 1 in the Supporting Information.[51] It can be seen from Figure 3a that for the Al disk the peak varies strongly with the surrounding medium, giving rise to very high theoretical sensitivity (1134 nm/RIU). Figure 3b shows that due to the absence of the field enhancement, the multiple features of the Si cylinder vary much less with the changing surrounding medium. This is also reflected in the low S values, which are an order of magnitude lower than that of the Al disk, Table SI 1. Finally, Figure 3c shows the response of the hybrid nanoantenna, which inherits multiple features from the Si cylinder but has much better sensitivity because it also benefits from the field enhancement of the metal disk. Such a system that exhibits multiple spectral features that vary differently upon interaction with the surrounding environment can bring advantages for sensing. However, it should also be noted that the S value of the hybrid nanoantenna is lower than that of the Al disk alone due to the interaction of the two subparts, as explained in the previous multipole analysis.

EXPERIMENTS

Next, we investigate the hybrid nanoantenna for bulk refractive index sensing with four different background media using a FTIR microscope (Bruker 80v FTIR spectrometer coupled with Hyperion 3000). The measurements are all done in transmission mode with the incident light oblique at a 16.7° angle of incidence with a 6.9° spread. We estimate that about 295 × 295 nanoantennas are probed simultaneously in the experiment. The experimental results are shown in Figure 4,

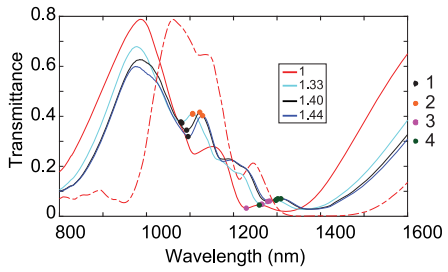

Figure 4. Experimental results for bulk refractive index sensing performed with the hybrid nanoantenna with four different glucose solutions as background. The red dashed curve shows the calculation for an air background (n = 1), scaled to the same magnitude as the experimental data.

where we clearly observe that the spectral features (either scattering minima or maxima) shift with the change of background refractive index. For all of the plots in Figure 4, an area without nanoantennas but with a similar background medium as the nanoantennas has been considered as reference. Table 1 shows the sensitivity values obtained from the

Table 1. Sensitivity Values Obtained from the Experiment and Corresponding Spectral Range

feature no.	$S = \Delta\lambda/\Delta n$ (nm/RIU)	range (nm)
1	144	1079−1095
2	208	1106−1129
3	120	1229−1283
4	111	1259−1309

experiment for different spectral features. Feature 2 gives the highest sensitivity value S = 208 nm/RIU. Figure 4 also includes the numerically calculated spectrum in air, which agrees quite well with the experimental data. Note that, contrary to the previous calculations used for the modes analysis, this calculation takes into account the periodic nature of the sample, the substrate, and the tilted illumination and mimics the numerical aperture used in the experiment by integrating all of the light that is collected by the objective.[52] The wider resonances obtained experimentally compared to the simulations originate from inhomogeneous broadening caused by fabrication variations over the sample area.

NANOANTENNA WITH AN UNDERCUT

The spatial overlap between the near-field of the structure and the analyte is important for refractive index sensing.[53−55] If we calculate the intensity distribution around the hybrid nanoantenna, we observe that due to the boundary conditions imposed by Maxwell's equations the area with strongest field intensity is buried inside the dielectric spacer and thus inaccessible to the analyte, Figure 5c. To allow the analyte access the region of high electromagnetic field, an undercut in the spacer region is proposed, Figure 5a.[56−58]

The undercut decreases the effective refractive index of the spacer region, which modifies the field distribution, and pushes out more field into the analyte, thus increasing their

https://dx.doi.org/10.1021/acs.nanolett.0c03613
Nano Lett. 2020, 20, 8752−8759

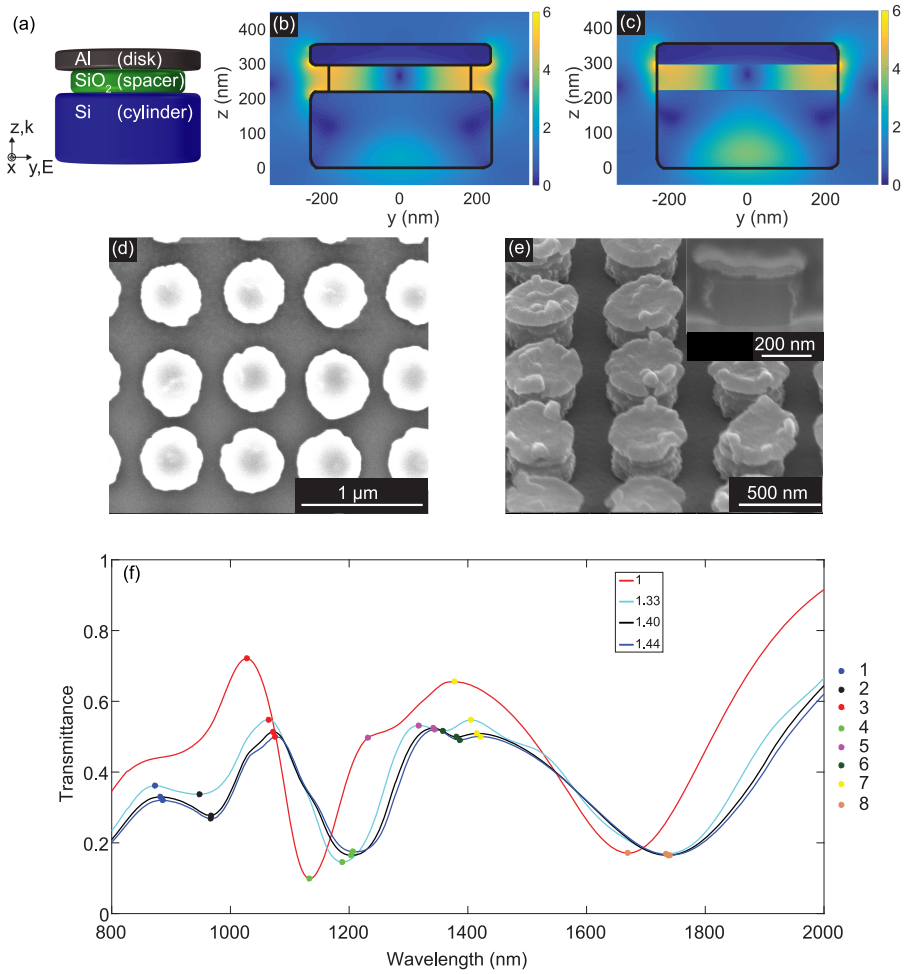

Figure 5. (a) Geometry of the hybrid nanoantenna with 50 nm undercut in SiO_2. Surface plots of electric field amplitude enhancement (the amplitude of the incident field is 1) in the *yz* plane for a periodic array of hybrid nanoantennas (b) with and (c) without a 50 nm undercut in the SiO_2. The outline of the nanoantenna is indicated in black. (d) Top view SEM image of the hybrid nanoantenna array with a period of 670 nm. (e) SEM image of the hybrid nanoantenna array imaged at a tilt of 52° to evidence the undercut in the SiO_2 spacer. The inset shows the cross-section made by FIB for a single nanoantenna. (f) Experimental transmittance for bulk refractive index sensing performed with hybrid nanoantenna with a 50 nm undercut in the SiO_2 for four different background conditions.

interaction, Figure 5b; compare Figure 5b and c. These calculations were performed for a periodic array of antennas in air at the wavelength corresponding to the main absorption peak λ = 1142 nm for the antenna without undercut and λ = 1122 nm for the antenna with an undercut. Both structures provide a similar field amplitude enhancement of the order of 6 times, but this enhanced field is clearly outside the structure in the case of an undercut, while it remains buried within the dielectric spacer without an undercut. Readers versed in the boundary conditions of Maxwell's equations might be surprised that the electric field appears continuous as it crosses the spacer interface in Figure 5b, although the incident field is along the *y*-direction, that is, normal to that interface. The reason for this is that the total field between the Si cylinder and the Al disk is dominantly polarized in the *z*-direction, as indicated in Figure SI 1.

The proposed nanoantenna with an undercut can be fabricated with an additional step of hydrofluoric acid (HF) vapor phase etching after the completion of the hybrid nanoantennas. The nanoantennas were etched for around 33 min at an average pressure of 67 Torr, Figure 5d. The 10 nm Al_2O_3 deposited on the fused silica substrate at the beginning of the fabrication protects the fused silica substrate from being etched during this step. The inset in Figure 5e shows a cross-section made by focused ion beam (FIB) on a single nanoantenna. The three layers, with an undercut in the SiO_2 can be seen from the cross-section as well as from Figure 5e. The latter demonstrates that hybrid nanoantennas with an undercut in the SiO_2 spacer have been successfully fabricated on a large area. We note that the top Al layer is quite grainy; this is very hard to avoid using a lift-off process.[32] Fortunately, this vertical roughness has limited influence on the response of the structure.

We investigate undercut structures for bulk refractive index sensing under similar conditions as those used in Figure 4. The results in Figure 5f show that due to the removal of the spacer region their spectral features are very different compared to the nanostructures without an undercut. We identify eight different spectral features and feature 5 gives the highest sensitivity with a value of 245 nm/RIU. Table 2 shows the sensitivity values calculated from the experiment. It can be seen from Figure 4 and Figure 5f that the undercut produces a modest improvement in the sensitivity in the order of 40 nm/RIU due to enhanced interaction of the analyte with the electric

https://dx.doi.org/10.1021/acs.nanolett.0c03613
Nano Lett. 2020, 20, 8752−8759

Table 2. Sensitivity Values Obtained from the Experiment and Corresponding Spectral Range for Nanoantennas with 50 nm Undercut

feature no.	$S = \Delta\lambda/\Delta n$ (nm/RIU)	range (nm)
1	110	873−886
2	153	948−968
3	110	1027−1075
4	169	1133−1206
5	245	1232−1344
6	169	1358−1387
7	98	1378−1422
8	167	1669−1740

field. Although the enhancement is smaller than that associated with substrate effects,[59] such an undercut would certainly be favorable for surface sensing as it will allow a few monolayers of the molecules to fully access the hotspot.[57] Surface functionalization of Al can be performed by silanization.[39,60]

CONCLUSIONS

In conclusion, to benefit from the strengths of plasmonics and dielectrics we have introduced a new fabrication friendly hybrid nanoantenna made out of Al and Si materials in a layered stack (sandwich) geometry. We have explained the working principle of the hybrid metal-dielectric nanostructure by multipolar decomposition. Such nanoantennas are fabricated uniformly over large areas and used for bulk refractive index sensing with a sensitivity of 208 nm/RIU. To increase the overlap between the electric field and the background medium, a 50 nm undercut was introduced in the SiO_2 spacer, which increased the sensitivity to 245 nm/RIU and provided additional spectral features, compared to the antennas without undercut. The hybrid nanostructure developed in this work could also be used for surface sensing or for fluorescence enhancement.

ASSOCIATED CONTENT

Supporting Information

The Supporting Information is available free of charge at https://pubs.acs.org/doi/10.1021/acs.nanolett.0c03613.

Table showing the simulated sensitivity value of a single nanoantenna (corresponding to Figure 3) and a plot showing the E distribution (corresponding to Figure 5b) (PDF)

AUTHOR INFORMATION

Corresponding Author

Olivier J. F. Martin − *Nanophotonics and Metrology Laboratory, Swiss Federal Institute of Technology Lausanne (EPFL), 1015 Lausanne, Switzerland;* orcid.org/0000-0002-9574-3119; Email: olivier.martin@epfl.ch

Authors

Debdatta Ray − *Nanophotonics and Metrology Laboratory, Swiss Federal Institute of Technology Lausanne (EPFL), 1015 Lausanne, Switzerland;* orcid.org/0000-0003-4817-9153

T. V. Raziman − *Nanophotonics and Metrology Laboratory, Swiss Federal Institute of Technology Lausanne (EPFL), 1015 Lausanne, Switzerland;* orcid.org/0000-0002-7085-6934

Christian Santschi − *Nanophotonics and Metrology Laboratory, Swiss Federal Institute of Technology Lausanne (EPFL), 1015 Lausanne, Switzerland*

Dordaneh Etezadi − *Bionanophotonic Systems Laboratory, Swiss Federal Institute of Technology Lausanne (EPFL), 1015 Lausanne, Switzerland;* orcid.org/0000-0003-4289-2476

Hatice Altug − *Bionanophotonic Systems Laboratory, Swiss Federal Institute of Technology Lausanne (EPFL), 1015 Lausanne, Switzerland;* orcid.org/0000-0001-5522-1343

Complete contact information is available at: https://pubs.acs.org/10.1021/acs.nanolett.0c03613

Notes

The authors declare no competing financial interest.

ACKNOWLEDGMENTS

It is a pleasure to acknowledge stimulating discussions with G. D Bernasconi. D.R. acknowledges the Swiss Government Excellence Scholarship; part of this work was funded by the Swiss National Science Foundation (project 200021_162453), the European Research Council (ERC-2015-AdG-695206 Nanofactory), European Research Council (ERC) under Grant Agreement 682167 VIBRANT-BIO project, and European Union Horizon 2020 Framework Programme for Research and Innovation under Grant Agreement 777714 (NOCTURNO project). We also acknowledge the Center of Mictrotechnology (CMi) in EPFL for providing the tools for nanofabrication.

REFERENCES

(1) Wang, J.; Du, J. Plasmonic and Dielectric Metasurfaces Design, Fabrication and Applications. *Appl. Sci.* **2016**, *6*, 239.

(2) Monticone, F.; Alú, A. Metamaterial, plasmonic and nanophotonic devices. *Rep. Prog. Phys.* **2017**, *80*, 036401.

(3) Kottmann, J. P.; Martin, O. J. F.; Smith, D. R.; Shultz, S. Field polarization and polarization charge distributions in plasmon resonant nanoparticles. *New J. Phys.* **2000**, *2*, 27.

(4) Yang, Y.; Kravchenko, I. I.; Briggs, D. P.; Valentine, J. All-dielectric metasurface analogue of electromagnetically induced transparency. *Nat. Commun.* **2014**, *5*, 5753.

(5) Li, S. V.; Baranov, D. G.; Krasnok, A. E.; Belov, P. A. All-dielectric nanoantennas for unidirectional excitation of electromagnetic guided modes. *Appl. Phys. Lett.* **2015**, *107*, 171101.

(6) Regmi, R.; Berthelot, J.; Winkler, P. M.; Mivelle, M.; Proust, J.; Bedu, F.; Ozerov, I.; Begou, T.; Lumeau, J.; Rigneault, H.; García-Parajó, M. F.; Bidault, S.; Wenger, J.; Bonod, N. All-Dielectric Silicon Nanogap Antennas To Enhance the Fluorescence of Single Molecules. *Nano Lett.* **2016**, *16*, 5143−5151.

(7) Bontempi, N.; Chong, K. E.; Orton, H. W.; Staude, I.; Choi, D.-Y.; Alessandri, I.; Kivshar, Y. S.; Neshev, D. N. Highly sensitive biosensors based on all-dielectric nanoresonators. *Nanoscale* **2017**, *9*, 4972−4980.

(8) Tittl, A.; Leitis, A.; Liu, M.; Yesilkoy, F.; Choi, D.-Y.; Neshev, D. N.; Kivshar, Y. S.; Altug, H. Imaging-based molecular barcoding with pixelated dielectric metasurfaces. *Science* **2018**, *360*, 1105.

(9) Devilez, A.; Stout, B.; Bonod, N. Compact Metallo-Dielectric Optical Antenna for Ultra Directional and Enhanced Radiative Emission. *ACS Nano* **2010**, *4*, 3390−3396.

(10) Zeng, X.; Yu, W.; Yao, P.; Xi, Z.; Lu, Y.; Wang, P. Metallo-dielectric hybrid antenna for high Purcell factor and radiation efficiency. *Opt. Express* **2014**, *22*, 14517−14523.

(11) Sun, S.; Zhang, T.; Liu, Q.; Ma, L.; Du, Q.; Duan, H. Enhanced Directional Fluorescence Emission of Randomly Oriented Emitters

via a Metal-Dielectric Hybrid Nanoantenna. *J. Phys. Chem. C* **2019**, *123*, 21150−21160.
(12) Sun, S.; Li, M.; Du, Q.; Png, C. E.; Bai, P. Metal-Dielectric Hybrid Dimer Nanoantenna: Coupling between Surface Plasmons and Dielectric Resonances for Fluorescence Enhancement. *J. Phys. Chem. C* **2017**, *121*, 12871−12884.
(13) Sun, S.; Li, R.; Li, M.; Du, Q.; Png, C. E.; Bai, P. Hybrid Mushroom Nanoantenna for Fluorescence Enhancement by Matching the Stokes Shift of the Emitter. *J. Phys. Chem. C* **2018**, *122*, 14771−14780.
(14) Rusak, E.; Staude, I.; Decker, M.; Sautter, J.; Miroshnichenko, A. E.; Powell, D. A.; Neshev, D. N.; Kivshar, Y. S. Hybrid nanoantennas for directional emission enhancement. *Appl. Phys. Lett.* **2014**, *105*, 221109.
(15) Guo, R.; Rusak, E.; Staude, I.; Dominguez, J.; Decker, M.; Rockstuhl, C.; Brener, I.; Neshev, D. N.; Kivshar, Y. S. Multipolar Coupling in Hybrid Metal Dielectric Metasurfaces. *ACS Photonics* **2016**, *3*, 349−353.
(16) Ho, J.; Fu, Y. H.; Dong, Z.; Paniagua-Dominguez, R.; Koay, E. H. H.; Yu, Y. F.; Valuckas, V.; Kuznetsov, A. I.; Yang, J. K. W. Highly Directive Hybrid Metal-Dielectric Yagi-Uda Nanoantennas. *ACS Nano* **2018**, *12*, 8616−8624.
(17) Tong, L.; Pakizeh, T.; Feuz, L.; Dmitriev, A. Highly directional bottom-up 3D nanoantenna for visible light. *Sci. Rep.* **2013**, *3*, 2311.
(18) Yang, G.; Niu, Y.; Wei, H.; Bai, B.; Sun, H.-B. Greatly amplified spontaneous emission of colloidal quantum dots mediated by a dielectric-plasmonic hybrid nanoantenna. *Nanophotonics* **2019**, *8*, 2313.
(19) Yue, W.; Song, G.; Sang-Shin, L.; Eun-Soo, K.; Duk-Yong, C. Subtractive Color Filters Based on a Silicon-Aluminum Hybrid-Nanodisk Metasurface Enabling Enhanced Color Purity. *Sci. Rep.* **2016**, *6*, 29756.
(20) Gili, V. F.; et al. Metal-dielectric hybrid nanoantennas for efficient frequency conversion at the anapole mode. *Beilstein J. Nanotechnol.* **2018**, *9*, 2306−2314.
(21) Shibanuma, T.; Grinblat, G.; Albella, P.; Maier, S. A. Efficient Third Harmonic Generation from Metal-Dielectric Hybrid Nanoantennas. *Nano Lett.* **2017**, *17*, 2647−2651.
(22) Hentschel, M.; Metzger, B.; Knabe, B.; Buse, K.; Giessen, H. Linear and nonlinear optical properties of hybrid metallic-dielectric plasmonic nanoantennas. *Beilstein J. Nanotechnol.* **2016**, *7*, 111−120.
(23) Brown, L. V.; Sobhani, H.; Lassiter, J. B.; Nordlander, P.; Halas, N. J. Heterodimers: Plasmonic Properties of Mismatched Nanoparticle Pairs. *ACS Nano* **2010**, *4*, 819−832.
(24) Sheikholeslami, S. N.; Garciá-Etxarri, A.; Dionne, J. A. Controlling the Interplay of Electric and Magnetic Modes via Fano-like Plasmon Resonances. *Nano Lett.* **2011**, *11*, 3927−3934.
(25) Flauraud, V.; Bernasconi, G. D.; Butet, J.; Alexander, D. T. L.; Martin, O. J. F.; Brugger, J. Mode Coupling in Plasmonic Heterodimers Probed with Electron Energy Loss Spectroscopy. *ACS Nano* **2017**, *11*, 3485−3495.
(26) Oldenburg, S. J.; Averitt, R. D.; Westcott, S. L.; Halas, N. J. Nanoengineering of optical resonances. *Chem. Phys. Lett.* **1998**, *288*, 243−247.
(27) Ghosh Chaudhuri, R.; Paria, S. Core/Shell Nanoparticles: Classes, Properties, Synthesis Mechanisms, Characterization, and Applications. *Chem. Rev.* **2012**, *112*, 2373−2433.
(28) Vala, M.; Etheridge, S.; Roach, J. A.; Homola, J. Long-range surface plasmons for sensitive detection of bacterial analytes. *Sens. Actuators, B* **2009**, *139*, 59−63.
(29) Špačková, B.; Wrobel, P.; Bocková, M.; Homola, J. Optical Biosensors Based on Plasmonic Nanostructures: A Review. *Proc. IEEE* **2016**, *104*, 2380−2408.
(30) Homola, J.; Yee, S. S.; Gauglitz, G. Surface plasmon resonance sensors: review. *Sens. Actuators, B* **1999**, *54*, 3−15.
(31) Piliarik, M.; Homola, J. Surface plasmon resonance (SPR) sensors: approaching their limits? *Opt. Express* **2009**, *17*, 16505−16517.
(32) Thyagarajan, K.; Santschi, C.; Langlet, P.; Martin, O. J. F. Highly Improved Fabrication of Ag and Al Nanostructures for UV and Nonlinear Plasmonics. *Adv. Opt. Mater.* **2016**, *4*, 871−876.
(33) Wang, Y.; Zhou, J.; Li, J. Construction of Plasmonic Nano-Biosensor-Based Devices for Point-of-Care Testing. *Small Methods* **2017**, *1*, 1700197.
(34) Claes, T.; Molera, J. G.; Vos, K. D.; Schacht, E.; Baets, R.; Bienstman, P. Label-Free Biosensing With a Slot-Waveguide-Based Ring Resonator in Silicon on Insulator. *IEEE Photonics J.* **2009**, *1*, 197−204.
(35) Yavas, O.; Svedendahl, M.; Dobosz, P.; Sanz, V.; Quidant, R. On-a-chip Biosensing Based on All-Dielectric Nanoresonators. *Nano Lett.* **2017**, *17*, 4421−4426.
(36) Steglich, P.; Villringer, C.; Pulwer, S.; Heinrich, F.; Bauer, J.; Dietzel, B.; Mai, C.; Mai, A.; Casalboni, M.; Schrader, S. Hybrid-Waveguide Ring Resonator for Biochemical Sensing. *IEEE Sens. J.* **2017**, *17*, 4781−4790.
(37) Naik, G. V.; Shalaev, V. M.; Boltasseva, A. Alternative Plasmonic Materials: Beyond Gold and Silver. *Adv. Mater.* **2013**, *25*, 3264−3294.
(38) Knight, M. W.; King, N. S.; Liu, L.; Everitt, H. O.; Nordlander, P.; Halas, N. J. Aluminum for Plasmonics. *ACS Nano* **2014**, *8*, 834−840.
(39) Li, W.; Ren, K.; Zhou, J. Aluminum-based localized surface plasmon resonance for biosensing. *TrAC, Trends Anal. Chem.* **2016**, *80*, 486−494.
(40) Dabos, G.; Manolis, A.; Tsiokos, D.; Ketzaki, D.; Chatzianagnostou, E.; Markey, L.; Rusakov, D.; Weeber, J.-C.; Dereux, A.; Giesecke, A.-L.; Porschatis, C.; Wahlbrink, T.; Chmielak, B.; Pleros, N. Aluminum plasmonic waveguides co-integrated with Si3N4 photonics using CMOS processes. *Sci. Rep.* **2018**, *8*, 13380.
(41) John-Herpin, A.; Tittl, A.; Altug, H. Quantifying the Limits of Detection of Surface-Enhanced Infrared Spectroscopy with Grating Order-Coupled Nanogap Antennas. *ACS Photonics* **2018**, *5*, 4117−4124.
(42) Etezadi, D.; Warner, J. B.; Lashuel, H. A.; Altug, H. Real-Time In Situ Secondary Structure Analysis of Protein Monolayer with Mid-Infrared Plasmonic Nanoantennas. *ACS Sensors* **2018**, *3*, 1109−1117.
(43) Pierce, D. T.; Spicer, W. E. Electronic Structure of Amorphous Si from Photoemission and Optical Studies. *Phys. Rev. B* **1972**, *5*, 3017−3029.
(44) Kern, A. M.; Martin, O. J. F. Surface integral formulation for 3D simulations of plasmonic and high permittivity nanostructures. *J. Opt. Soc. Am. A* **2009**, *26*, 732−740.
(45) Raziman, T. V.; Somerville, W. R. C.; Martin, O. J. F.; Le Ru, E. C. Accuracy of surface integral equation matrix elements in plasmonic calculations. *J. Opt. Soc. Am. B* **2015**, *32*, 485−492.
(46) Mühlig, S.; Menzel, C.; Rockstuhl, C.; Lederer, F. Multipole analysis of meta-atoms. *Metamaterials* **2011**, *5*, 64−73.
(47) Yan, C.; Wang, X.; Raziman, T. V.; Martin, O. J. F. Twisting Fluorescence through Extrinsic Chiral Antennas. *Nano Lett.* **2017**, *17*, 2265−2272.
(48) Alaee, R.; Rockstuhl, C.; Fernandez-Corbaton, I. Exact Multipolar Decompositions with Applications in Nanophotonics. *Adv. Opt. Mater.* **2019**, *7*, 1800783.
(49) Staude, I.; Miroshnichenko, A. E.; Decker, M.; Fofang, N. T.; Liu, S.; Gonzales, E.; Dominguez, J.; Luk, T. S.; Neshev, D. N.; Brener, I.; Kivshar, Y. Tailoring Directional Scattering through Magnetic and Electric Resonances in Subwavelength Silicon Nanodisks. *ACS Nano* **2013**, *7*, 7824−7832.
(50) Kiselev, A.; Bernasconi, G. D.; Martin, O. J. F. Modes interplay and dynamics in the second harmonic generation of plasmonic nanostructures. *Opt. Express* **2019**, *27*, 38708−38720.
(51) Unger, A.; Kreiter, M. Analyzing the Performance of Plasmonic Resonators for Dielectric Sensing. *J. Phys. Chem. C* **2009**, *113*, 12243−12251.
(52) Gallinet, B.; Kern, A. M.; Martin, O. J. F. Accurate and versatile modeling of electromagnetic scattering on periodic nanostructures

https://dx.doi.org/10.1021/acs.nanolett.0c03613
Nano Lett. 2020, 20, 8752−8759

with a surface integral approach. *J. Opt. Soc. Am. A* **2010**, *27*, 2261−2271.
(53) Vollmer, F.; Arnold, S.; Keng, D. Single virus detection from the reactive shift of a whispering-gallery mode. *Proc. Natl. Acad. Sci. U. S. A.* **2008**, *105*, 20701−20704.
(54) Santiago-Cordoba, M. A.; Boriskina, S. V.; Vollmer, F.; Demirel, M. C. Nanoparticle-based protein detection by optical shift of a resonant microcavity. *Appl. Phys. Lett.* **2011**, *99*, 073701.
(55) Zhang, W.; Martin, O. J. F. A Universal Law for Plasmon Resonance Shift in Biosensing. *ACS Photonics* **2015**, *2*, 144−150.
(56) Brian, B.; Sepúlveda, B.; Alaverdyan, Y.; Lechuga, L. M.; Käll, M. Sensitivity enhancement of nanoplasmonic sensors in low refractive index substrates. *Opt. Express* **2009**, *17*, 2015−2023.
(57) Otte, M. A.; Estévez, M.-C.; Carrascosa, L. G.; González-Guerrero, A. B.; Lechuga, L. M.; Sepúlveda, B. Improved Biosensing Capability with Novel Suspended Nanodisks. *J. Phys. Chem. C* **2011**, *115*, 5344−5351.
(58) Huck, C.; Toma, A.; Neubrech, F.; Chirumamilla, M.; Vogt, J.; De Angelis, F.; Pucci, A. Gold Nanoantennas on a Pedestal for Plasmonic Enhancement in the Infrared. *ACS Photonics* **2015**, *2*, 497−505.
(59) Dmitriev, A.; Hagglund, C.; Chen, S.; Fredriksson, H.; Pakizeh, T.; Kall, M.; Sutherland, D. S. Enhanced Nanoplasmonic Optical Sensors with Reduced Substrate Effect. *Nano Lett.* **2008**, *8*, 3893−3898.
(60) Tian, S.; Neumann, O.; McClain, M. J.; Yang, X.; Zhou, L.; Zhang, C.; Nordlander, P.; Halas, N. J. Aluminum Nanocrystals: A Sustainable Substrate for Quantitative SERS-Based DNA Detection. *Nano Lett.* **2017**, *17*, 5071−5077.

https://dx.doi.org/10.1021/acs.nanolett.0c03613
Nano Lett. 2020, 20, 8752−8759